Altshuler-Aronov effects in nonequilibrium disordered nanostructures

Chenyi Zhou* and Hong Guo
Center for the Physics of Materials and Department of Physics, McGill University, Montréal, Canada, H3A 2T8

(Received 3 May 2019; revised manuscript received 17 June 2019; published 18 July 2019)

The Altshuler-Aronov (AA) effect is one of the most basic quantum many-body effects in the mesoscopic regime. It originates from the coexistence of disorder and electron-electron interaction. In this paper, we reformulate the Feynman diagrammatic theory of the AA effect in a real-space nonequilibrium Green's function framework, in which an effective medium technique (via coherent potential) is employed to evaluate disorder-induced vertices in the diagrams. As such the developed real-space formalism is compatible with the prevailing nanodevice simulation paradigm, leading to an effective numerical approach to calculating the AA effects on electronic structures and quantum transport properties of nanostructures. As an application, we analyze the I-V characteristics and the full local density of states (DOS) profile of an Anderson-Hubbard lattice sandwiched between biased electrodes. We show how the DOS anomaly due to the AA mechanism is reshaped by the geometrical confinement and the nonequilibrium effects in a nanosystem. Our numerical findings are well understood by the analytical results we provide in this paper.

DOI: 10.1103/PhysRevB.100.045413

I. INTRODUCTION

Disorder and pair interaction are the two scattering sources most elementary in a many-electron system. Their various effects, and especially the interplay between them [1,2], play a central role in the basic understanding of quantum condensed matter. Quantum transport in the absence of electron-electron (e-e) interaction is essentially a single-particle problem. It is well understood that macroscopic quantum diffusion is prohibited in low-dimensional ($d \leqslant 2$) systems with an arbitrary concentration of impurities [3] and that, in the mesoscopic regime, such localization effect reduces to a subleading correction, the weak localization [4], to the dominant diffusion process. Another quantum correction to diffusive transport arises from the e-e interaction: The spatial charge fluctuation induced by impurities acts as an additional source of scattering, and its combined effect with the electron-impurity scattering forms a further suppression of the electronic conductivity [5]. This effect was first theoretically analyzed by Altshuler and Aronov (AA) using a many-body diagrammatic method in the linear response framework [6]. Furthermore, it was found that the same physical picture gave rise to a strong suppression of the density of states (DOS) at the Fermi energy [6], which was verified by tunneling spectroscopy studies of dirty metallic contacts [7]. In this paper, the interaction induced quantum corrections to conductance and DOS of *disordered systems* are referred to as the AA effect [6].

While there is a great amount of literature focusing on AA effects in the *linear* transport regime, it has been less discussed how the AA mechanism reshapes the nonlinear current-voltage (I-V) curves and the (local) DOS profiles of geometrically confined systems (e.g., nanostructures). The latter problem is of great relevance to the constantly rising interest in nanodevices, whose nonlinear transport features and electronic structures need to be thoroughly understood for engineering applications. Theoretical developments in this direction were initiated by Nagaev [8] who analytically derived an expression for the nonlinear current in diffusive metallic contacts, using diagrammatic perturbation theory. With a quasiclassical approach, Schwab *et al.* [9] analyzed nonlinear transport in nanostructures of a few geometries. Concerning the AA effect on DOS, Gutman *et al.* [10] suggested from their matrix field analysis that the cusp structure in the DOS profile should split in two under nonlinear condition. Within specifically chosen models, these theoretical works provided important understandings of different aspects of the AA effect.

In this work, we wish to put forward a unified formalism which is consistent with existing theoretical findings while extending the realm of applying the renowned AA theory. To be specific, we focus on reformulating the AA diagrams using the nonequilibrium Green's function (NEGF) theory. As such the developed real-space formalism is compatible with the prevailing nanodevice simulation paradigm, leading to an effective numerical approach to calculating the AA effects on electronic structures and quantum transport properties of nanostructures. Associated with this formalism, we propose a generic form of disorder-averaging technique in terms of the diagrammatics, which improves the transferability of the diagrammatic theory. The theory developed in this paper works in conjunction with numerical Hamiltonians constructed with localized basis sets, thereby complying with the state-of-the-art nanodevice simulation framework [11,12] which supports the bottom-up device modeling in real space. In addition, the numerical model accepts arbitrary configurations of substitutional disorder. This is achieved by using the coherent potential approximation (CPA) [13,14] to compute the disorder-induced vertices in our diagrammatics. The use of CPA is especially advantageous to *ab initio* implementations for real materials.

*Corresponding author: zhouc@physics.mcgill.ca

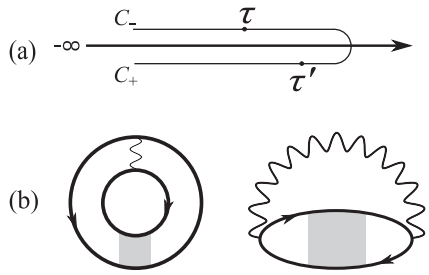

FIG. 1. (a) Keldysh contour. (b) Free energy diagrams to the first order in e-e interaction (wavy line). The gray area in each diagram represents the disorder vertex induced by configuration average.

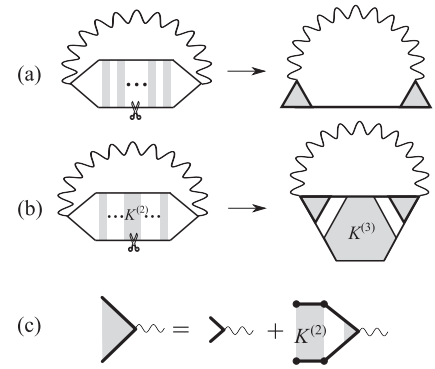

FIG. 2. Demonstration of the Kadanoff-Baym scheme for deriving self-energies (a),(b). Here the Fock (exchange) diagram is used for example. The Hartree self-energy can be derived in a similar manner. (c) displays the recursive structure of the vertex correction.

A common theoretical issue in transport formalisms is whether the formula for computing charge currents respects charge conservation. If not, the theory would be considered incomplete. In the literature Ref. [8] and in Sec. III B below, there are situations where the *approximate* current formula explicitly depends on the spatial coordinate, which would in principle violate charge conservation. This problem is fixed in our numerical formalism by applying additional vertex corrections in the NEGF framework, and hence we obtain a scheme that yields the same current at any cross section of the device.

This paper is organized as follows. In Sec. II we review the NEGF formalism and present the essential Feynman diagrams which lead to the AA effects. In Sec. III we present the analytical results obtained under the diffusive approximation and at the Hartree-Fock level. These results apply to the scenario of a short diffusive conductor sandwiched between nonequilibrium electrodes, which corresponds to the typical nanotransport setup. In particular, both the spatial and the energy dependences of the local DOS in such a system are analyzed. We also derive a compact formula for calculating the nonlinear charge current therein. These analytical results will be used to understand our numerical findings. In Sec. IV we introduce an Anderson-Hubbard model of tight-binding form, which can be viewed as a prototype for real *ab initio* simulations. We also provide additional technical details about our numerical scheme, especially about how the disorder-induced vertices are computed with CPA. Applications of our formalism to a one-dimensional transport structure are reported. In particular, we find in its local DOS an interesting spatial dependence that arises from the geometrical confinement in the transport (longitudinal) direction. We will also briefly discuss the energy relaxation effect on the DOS profile due to inelastic e-e scattering.

II. MANY-BODY TECHNIQUE: AN OVERVIEW

In this section we outline the NEGF technique and its associated many-body diagrammatics for analyzing general disordered interacting systems, as these theories will be needed in the rest of the developments below. We start by drawing the two free energy diagrams to the first order in the e-e interaction [see Fig. 1(b)]. The interaction vertex is represented by the wavy lines in the graph, and the arrowed lines denote contour-ordered Green's functions $G(\mathbf{r}\tau, \mathbf{r}'\tau') = -\mathrm{i}\langle T_C \psi(\mathbf{r}\tau)\psi^\dagger(\mathbf{r}'\tau')\rangle$ where the complex-time arguments τ and τ' are placed on the Keldysh contour [see Fig. 1(a)] [15]. Note that spin degeneracy is assumed throughout this work.

The two Green's function lines in each diagram are further dressed by a four-point vertex in between, as a result of disorder average. It can be shown that this vertex can be expanded as a ladder series, i.e., $K^{(2)} + K^{(2)}(GG)K^{(2)} + K^{(2)}(GG)K^{(2)}(GG)K^{(2)} + \cdots$, where $K^{(2)}$ is a four-point function irreducible in the particle-hole channel [14,16]. Note that, although $K^{(2)}$ is commonly approximated as a local function in space, in principle it can be nonlocal, and its spatial nonlocality has a particular importance for describing quantum interference effects such as localization [16].

We then generate the consistent self-energy diagrams following the Baym-Kadanoff procedure [17], i.e., removing a Green's function line at an arbitrary place in each free energy diagram. Self-energies derived in this way can be shown to have desired conservation properties for transport calculations [14,17]. Depending on whether the Green's function is removed from inside an irreducible vertex $K^{(2)}$ or between two adjacent $K^{(2)}$'s, the resulting self-energy diagram may have either of the two structures as shown in Figs. 2(a) and 2(b). The total self-energy has to be the sum of these two types. Figure 2(a) can be viewed as a Fock diagram with the interaction vertex dressed by disorder-induced corrections (represented by the triangular objects in the diagram). The six-point vertex $K^{(3)}$ that shows up in Fig. 2(b) can be formally expressed as $\delta K^{(2)}/\delta G$ and is three-particle irreducible [14]. Having the appropriate self-energy (hereafter denoted by Σ), one can write down the first-order interaction-induced correction to the Green's function as $\delta G = G\Sigma G$, where convolutions in real space and complex time are implied on the right hand side.

In order to actually evaluate these diagrams, one resorts to the real-time Green's functions following the continuation procedure [18]:

$$G(\mathbf{r}_1\tau_1, \mathbf{r}_2\tau_2) \to \begin{cases} G^{--} & \tau_1, \tau_2 \in C_- \\ G^{+-} & \tau_1 \in C_+, \tau_2 \in C_- \\ G^{-+} & \tau_1 \in C_-, \tau_2 \in C_+ \\ G^{++} & \tau_1, \tau_2 \in C_+ \end{cases} \quad (1)$$

where $\tau_{1,2}$ are variables on the Keldysh contour in Fig. 1(a), and C_+, C_- indicate its backward and forward branches, respectively. This way the complex-time arguments are removed at the price of introducing more real-time Green's functions. It is then suggestive to arrange the four Green's functions in a matrix form

$$G^{ss'} = \begin{bmatrix} G^{--} & G^{-+} \\ G^{+-} & G^{++} \end{bmatrix} \tag{2}$$

where the additional index s marks the contour branch in which the original time argument was placed. Therefore, complex-time convolutions along the contour are now replaced with integrals along the real axis plus a sum over the branch index s. For numerically computing complex diagrams, the $G^{ss'}$ Green's functions turn out to be more convenient than the conventionally used retarded (R), advanced (A), and Keldysh (K) Green's functions [15], which can be introduced as

$$\begin{aligned} G^{\mathrm{R}} &= G^{--} - G^{-+}, \\ G^{\mathrm{A}} &= G^{--} - G^{+-}, \\ G^{\mathrm{K}} &= G^{-+} + G^{+-}, \end{aligned} \tag{3}$$

in the current formalism.

The interaction (hereafter denoted by U) should also be augmented in the form of Eq. (2). The relation between $U^{ss'}$ and $U^{\mathrm{R/A/K}}$ follows

$$\begin{aligned} U^{\mathrm{R}} &= U^{--} + U^{-+}, \\ U^{\mathrm{A}} &= U^{--} + U^{+-}, \\ U^{\mathrm{K}} &= -U^{-+} - U^{+-}, \end{aligned} \tag{4}$$

instead of Eq. (3). The sign differences arise from the need to take care of the opposite integration directions along the two contour branches. Also, note that each interaction line contributes a prefactor of i to the final value of the diagram. Under the nonequilibrium random phase approximation, the (screened) interaction is generated from [19]

$$U^{\mathrm{R/A}} = U_0 + U_0 P^{\mathrm{R/A}} U^{\mathrm{R/A}}, \tag{5a}$$

$$U^{\mathrm{K}} = U^{\mathrm{R}} P^{\mathrm{K}} U^{\mathrm{A}}, \tag{5b}$$

where U_0 is bare Coulomb interaction and P denotes polarization. When P is dressed due to disorder average, it would be easier to compute

$$P^{ss'}(\mathbf{r}t, \mathbf{r}'t') = -\mathrm{i}\langle G^{ss'}(\mathbf{r}t, \mathbf{r}'t') \cdot G^{s's}(\mathbf{r}'t', \mathbf{r}t) \rangle, \tag{6}$$

where $\langle \cdots \rangle$ denotes disorder average, and then transform $P^{ss'}$ to $P^{\mathrm{R/A/K}}$ using the same relation as in Eq. (3).

The diagrammatic rules regarding $G^{ss'}$, $U^{ss'}$, and $P^{ss'}$ (without disorder involved) are reviewed in Ref. [18]. The challenge in evaluating those diagrams of Fig. 2 lies in calculating the disorder related vertices, which will be further elaborated once our disorder-averaging scheme is specified (see below, Sec. IV B).

Finally, the self-energy is obtained by putting together all the diagrammatic building blocks and integrating over all internal variables in the diagrams. The relation between $\Sigma^{ss'}$ and $\Sigma^{\mathrm{R/A/K}}$ follows that of Eq. (4).

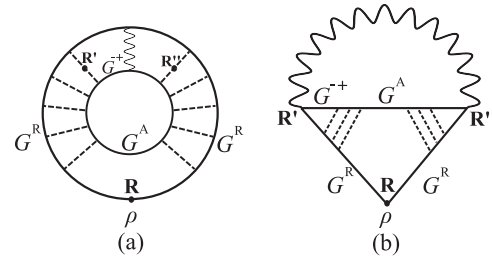

FIG. 3. Hartree (a) and Fock (b) diagrams for the interaction correction to the DOS of weakly disordered systems. The ladder series composed of dashed lines represents the diffuson objects. Boldface letters (e.g., **R**) indicate spatial coordinates on a macroscopic scale greater than the impurity mean free path.

III. THEORETICAL MODEL ANALYSIS

In this section, we provide analytical results of a nanowire model sandwiched between ideal electrodes. To facilitate the derivation, we assume a weak disorder scenario where the mean free path (l_0) of impurity scattering is much larger than the Fermi wavelength. As such, the four-point disorder vertex $K^{(2)}$ in the diagrammatics reduces to a dashed line, i.e., first Born approximation (see Fig. 3), which is local in the space and carries a value of $(2\pi \nu_0 \tau_0)^{-1}$ [20], ν_0 being the unperturbed DOS and τ_0 being the relaxation time of impurity scattering. We also assume a phase-coherent elastic e-e scattering, which preserves the most essential interference process associated with the AA effects.

Before getting into the analytical derivation, it would be helpful to review the various characteristic length scales in the problem. First, because of momentum relaxation, wave functions of single-particle states are confined in a spatial region bounded by l_0. However, the particle density could correlate in space over a distance much larger than l_0. This type of long-range correlation arises from the diffusion modes in the system and is usually characterized by a classical length scale $\sqrt{D/\omega}$, where D is the diffusion coefficient and ω is the frequency of the driving field. In the following, we shall see that the ratio between $\sqrt{D/\omega}$ and the sample size plays an important role in the interaction effect of DOS anomalies. At nonzero temperatures, there exists another diffusion length $\sqrt{\hbar D/k_B T}$. To simplify our analysis we set $T = 0$ by hand so that this thermal length becomes irrelevant. In addition to the diffusion, another long-range object could be the Coulomb interaction, whose spatial scope depends specifically on the charge carrier density and the system dimension. Nevertheless, it is essentially the diffusive motion of carriers that is responsible for the singularities in the interaction induced corrections, whereas different models of e-e interaction merely result in additional prefactors [6,20].

The above discussion was based on the interaction effect to the first order. If one were to go beyond this approximation level, other length scales, such as the energy relaxation length and the dephasing length [21], would come into the picture and further complicate the problem. For example, Ref. [10] predicts that in mesoscopic films the nonequilibrium electromagnetic noise due to inelastic scattering is responsible for smearing the DOS anomaly, and the sample size hence

becomes an irrelevant length scale instead of the dominant one as in the perturbation theory. These higher-order effects will not be considered in this section; they will be discussed in Sec. IV C by means of numerical investigation. Analytical results of this section apply to diffusive nanowires or metallic contacts where the dominant cutoff length scale is the longitudinal size (L) itself.

A. Density of states

The first-order DOS correction due to interaction can be written as $\delta\nu(\varepsilon) = -\frac{1}{\pi}\mathrm{Im}[G^{\mathrm{R}}\Sigma^{\mathrm{R}}G^{\mathrm{R}}]$, where G^{R} denotes the noninteracting (retarded) Green's function. Using the diagrammatic rules presented in Sec. II, we obtain Fig. 3 for evaluating $\delta\nu$ at the Hartree-Fock level. The types of the involved Green's functions are labeled on the graph. The retarded and advanced Green's functions are merely propagators of independent particles and thus do not contain any statistical information. The particle distribution $f(\varepsilon)$ gets involved via G^{-+}, which can be written as

$$G^{-+}(\varepsilon) \approx f(\varepsilon)[G^{\mathrm{A}}(\varepsilon) - G^{\mathrm{R}}(\varepsilon)] \tag{7}$$

in the form of the equilibrium fluctuation-dissipation theorem [19]. The nonequilibrium correction to Eq. (7) is of a higher order and thus will not be explicitly considered in our analytical derivation. For a uniformly disordered system subject to an external bias (along the $\hat{x}$ direction), the distribution function has the following linear form [8–10,22]:

$$f(\varepsilon, x) = f(\varepsilon, 0) + \frac{x}{L}[f(\varepsilon, L) - f(\varepsilon, 0)], \tag{8}$$

where L is the distance between electrodes. $f(\varepsilon, 0)$ and $f(\varepsilon, L)$ are Fermi-Dirac distributions in the respective electrodes, and they take the following simple forms at zero temperature: $f(\varepsilon, 0) = \Theta(eV/2 - \varepsilon)$ and $f(\varepsilon, L) = \Theta(-eV/2 - \varepsilon)$, where Θ denotes the Heaviside step function and V is the bias voltage.

In each diagram there are two blocks composed of a series of dashed lines. Each of them represents a diffuson which can be evaluated as $(2\pi\nu_0\tau_0^2)^{-1}\langle G^{\mathrm{R}}(\varepsilon)G^{\mathrm{A}}(\varepsilon-\omega)\rangle$. Note that the diagrams which involve products of the form $G^{\mathrm{R}}(\mathbf{r}_1, \mathbf{r}_2)G^{\mathrm{R}}(\mathbf{r}_2, \mathbf{r}_1)$ have been discarded in advance, because they carry a small factor of $(E_{\mathrm{F}}\tau_0)^{-1}$. On the other hand, the correlator $(2\pi\nu_0)^{-1}\langle G^{\mathrm{R}}G^{\mathrm{A}}\rangle$ (i.e., the diffuson, hereafter denoted by $\mathcal{P}$) can be shown to be independent on ε, and it equals the classical diffusion propagator in the long range [20]. Thus the diagrams are divided into three short-range regions by the two long-range diffusons, and the contribution from each region can hence be computed separately. These contributions only consist of some spatial convolutions between G^{R} or G^{A}, which can be evaluated by using the relation $G^{\mathrm{R}}(\varepsilon)G^{\mathrm{A}}(\varepsilon) = \mathrm{i}\tau_0[G^{\mathrm{R}}(\varepsilon) - G^{\mathrm{A}}(\varepsilon)]$. Collecting all the pieces of Fig. 3, we get

$$\delta\nu(\varepsilon\mathbf{R}) = -\frac{\nu_0}{\pi}\mathrm{Im}\int d\omega d\mathbf{R}' d\mathbf{R}'' \mathcal{P}(\mathbf{R}, \mathbf{R}', \omega) f(\varepsilon-\omega, \mathbf{R}') \times [U_0(\mathbf{R}'-\mathbf{R}'') - 2\mathcal{F}\bar{U}\delta(\mathbf{R}'-\mathbf{R}'')]\mathcal{P}(\mathbf{R}'', \mathbf{R}, \omega), \tag{9}$$

where the boldface $\mathbf{R}$ is used to stress that the spatial coordinates in this formula are based on a length scale greater than l_0. The numeric factor $\mathcal{F}$ induced from the Hartree diagram is a material parameter which is defined as

$$\mathcal{F} = \frac{\int [\mathrm{Im}G^{\mathrm{R}}(\mathbf{r})]^2 U_0(\mathbf{r}) d\mathbf{r}}{(\pi\nu_0)^2 \int U_0(\mathbf{r}) d\mathbf{r}}, \tag{10}$$

and $\bar{U} = \int U_0(\mathbf{r}) d\mathbf{r}$. Since $\mathrm{Im}G^{\mathrm{R}}(\mathbf{r})$ is a short-range function decaying in space, the value of $\mathcal{F}$ falls in between 0 and 1. For very strong screening, namely when the screening length is shorter than the Fermi wavelength, $\mathcal{F} = 1$, while in the opposite limit $\mathcal{F} = 0$ [20]. It is important to notice that the actual value of $\mathcal{F}$ affects the sign of $\delta\nu$. Evaluating Eq. (9) also requires the knowledge of $U_0(\mathbf{R}' - \mathbf{R}'')$. However, in nanostructures the effective e-e interaction depends on the specific device setup and thus can be very complicated in general. To proceed from Eq. (9), we adopt a local interaction of the form corresponding to static screening in metals [20]:

$$U_0(\mathbf{R}_1 - \mathbf{R}_2) = (2\nu_0)^{-1}\delta(\mathbf{R}_1 - \mathbf{R}_2). \tag{11}$$

The δ-function approximation is valid because the screening length is much shorter than l_0 in normal metals. Substituting Eq. (11) into Eq. (9), we obtain in one dimension

$$\delta\nu(\varepsilon, x) = \frac{2\mathcal{F}-1}{2\pi}\mathrm{Im}\int d\omega \int_0^L dx' f(\varepsilon-\omega, x') \times [\mathcal{P}(x, x', \omega)]^2. \tag{12}$$

The integral can be written in two parts:

$$\delta\nu = (1 - 2\mathcal{F})(\delta\nu_1 + \delta\nu_2), \tag{13}$$

where

$$\delta\nu_1(\varepsilon, x) = -\frac{1}{4\pi}\mathrm{Re}[\mathcal{P}_x(\varepsilon - eV/2) + \mathcal{P}_x(\varepsilon + eV/2)] \tag{14a}$$

$$\delta\nu_2(\varepsilon, x) = \mathrm{Im}\int_{\varepsilon-eV/2}^{\varepsilon+eV/2}\frac{d\omega}{2\pi}\int_0^L dx' \frac{x' - L/2}{L}[\mathcal{P}(x, x', \omega)]^2. \tag{14b}$$

To proceed we insert the classical solution of $\mathcal{P}$ subject to the Dirichlet boundary condition in one dimension, i.e.,

$$\mathcal{P}(x, x', \omega) = \frac{2}{L}\sum_{n>0}\frac{\sin(n\pi x/L)\sin(n\pi x'/L)}{\pi^2 n^2 D/L^2 - \mathrm{i}\omega} \tag{15}$$

$$= \frac{L_\omega}{D}\frac{\sinh(x_m/L_\omega)\sinh(L - x_M)/L_\omega}{\sinh(L/L_\omega)}, \tag{16}$$

where $x_m = \min(x, x')$, $x_M = \max(x, x')$, and $L_\omega = \sqrt{\mathrm{i}D/\omega}$ sets the length scale for a diffusion mode with frequency ω.

Let us first look at the first part $\delta\nu_1$ as defined in Eq. (14a), which is simply proportional to the recurrence probability $\mathrm{Re}\mathcal{P}_{x=x'}(\omega)$. Since $\mathrm{Re}\mathcal{P}_x(\omega)$ is an even function peaked at $\omega = 0$, $\delta\nu_1$ is symmetric in ε and has two cusps at $\varepsilon = \pm eV/2$ under an external bias. The cusp depth $\delta\nu_1(\pm eV/2)$ varies with x. To see this, we set ω at zero and hence obtain

$$\mathrm{Re}\mathcal{P}_x(\omega = 0) = \frac{x}{D}\left(1 - \frac{x}{L}\right). \tag{17}$$

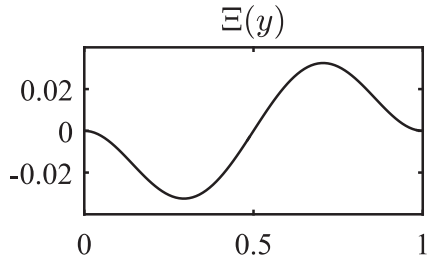

FIG. 4. Plot of the function $\Xi(y) = (1-2y)(y-1)^2y^2(4y^2 - 4y - 1)$, which we invoke in Eq. (20).

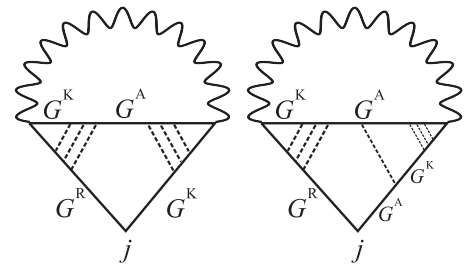

FIG. 5. Diagrams for the first-order interaction correction to the charge current in weakly disordered systems. Here only the Fock diagrams are shown, since those of Hartree can be obtained by simply rearranging the interaction vertex [see Fig. 3(a)].

Therefore $\delta\nu_1(\pm eV/2)$ is deepest at $x = L/2$, and around the cusp,

$$\delta\nu_1(\omega, L/2) = -\mathrm{Re}\left\{\frac{\tanh L/2L_\omega}{8\pi\sqrt{-i D\omega}}\right\}, \tag{18}$$

where $\omega = \varepsilon \pm eV/2$. On the contrary, $\delta\nu_1(\pm eV/2)$ vanishes at the ends of the wire. The underlying physical picture is that the closer particles get to the boundaries, the more tendency they will be absorbed by the reservoirs and never return to the interacting region.

At a fixed x/L ratio, $\delta\nu_1(\pm eV/2)$ is proportional to L. This implies a DOS singularity when the thermodynamic limit $L \to \infty$ is taken. To see this singularity on the energy axis, we set $x = x' = L/2$ at first and then get $\mathrm{Re}\mathcal{P}(\omega) = 1/\sqrt{8D\omega}$ from Eq. (16) in the limit $L \gg L_\omega$. Thus at equilibrium we have $\delta\nu_1(\varepsilon) = -(4\pi\sqrt{2D\varepsilon})^{-1}$, which reproduces the well-known "zero-bias anomaly" (as $\varepsilon \to 0$) first elucidated by Altshuler and Aronov [6]. In real materials, this singularity is usually cut off by certain finite length scales such as the thermal diffusion length $\sqrt{\hbar D/k_B T}$ or the dephasing length [6,10]. In the present work which mainly focuses on short wires, this anomaly is simply cut off by the system size [see Eq. (18)].

The second part $\delta\nu_2$ [see Eq. (14b)] exists only at nonequilibrium, and it contributes a subleading modulation on top of $\delta\nu_1$. The spatial integral in Eq. (14b) yields

$$\begin{aligned}\int_0^L dx' \frac{x' - L/2}{L}\left[\mathcal{P}(x, x', \omega)\right]^2 &= \frac{L_\omega^4}{8LD^2\sinh^2(L/L_\omega)}\left[\left(1 - \cosh\frac{2x}{L_\omega} - \frac{L-2x}{L_\omega}\sinh\frac{2x}{L_\omega}\right.\right.\\ &\left.\left. + \frac{2x(L-x)}{L_\omega^2}\right)\sinh^2\frac{L-x}{L_\omega} - (x \to (L-x))\right].\end{aligned} \tag{19}$$

However, the remaining ω integral cannot be performed analytically. To proceed we simplify the result of Eq. (19) in the low bias limit $eV \ll \hbar D/L^2$. The quantity $\hbar D/L^2$ is usually termed the Thouless energy (E_{Th}) in the literature. Expanding Eq. (19) with respect to the small parameter L/L_ω and next completing the frequency integral, we get

$$\delta\nu_2(\varepsilon, x) \approx \frac{eVL^5}{360\pi D^3}\varepsilon\,\Xi(x/L), \quad eV \ll E_{\mathrm{Th}}, \tag{20}$$

where Ξ is a polynomial as shown in Fig. 4. We notice that $\Xi(x/L)$, as well as $\delta\nu_2$, is an odd function with respect to $x = L/2$, and that it vanishes at $x = 0, L$. This particular x dependence is in fact a generic property which can be easily deduced from Eq. (19). In addition, $\delta\nu_2$ is also an odd function of ε, which can be deduced from Eq. (15) since flipping the sign of ω is equivalent to taking the conjugate. If we are only concerned about the $\delta\nu_2$ value around the cusps, i.e., $\delta\nu_2(\pm|\eta + eV/2|)$, we can alternatively apply the nonlinear limit $L \gg L_\omega$ to Eq. (19), which then reduces to $L_\omega^3(2x - L)/(8LD^2)$ for $0 < |x - L/2| < L/2$. As such, we get

$$\delta\nu_2(\pm|\eta + eV/2|, x) \approx \pm\frac{2x - L}{8\pi L\sqrt{2D\eta}}, \; E_{\mathrm{Th}} \ll \eta \ll eV. \tag{21}$$

Therefore, both the linear and the nonlinear results suggest that the DOS correction should have a profile such that $|\delta\nu(eV/2, x)|$ is greater (lesser) than $|\delta\nu(-eV/2, x)|$ if $x < L/2$ ($x > L/2$). This point will be verified by our numerical simulation (see Fig. 13 below).

B. Charge current

The nonequilibrium charge current can be obtained from the Keldysh Green's function [8]:

$$j(\mathbf{r}) = \frac{e\hbar}{4\pi m}\int d\varepsilon \lim_{\mathbf{r}'\to\mathbf{r}}\left(\nabla' - \nabla\right)G^{\mathrm{K}}(\mathbf{r}, \mathbf{r}', \varepsilon). \tag{22}$$

The interaction induced correction to G^{K} can be expressed as $\delta G^{\mathrm{K}} = G^{\mathrm{R}}\Sigma^{\mathrm{R}}G^{\mathrm{K}} + G^{\mathrm{K}}\Sigma^{\mathrm{A}}G^{\mathrm{A}} + G^{\mathrm{R}}\Sigma^{\mathrm{K}}G^{\mathrm{A}}$. Putting aside the terms involving U^{K} for now, i.e., the dynamic part which plays a role only in the subleading dephasing effects [23], one obtains the diagrams of Fig. 5 (together with their Hartree counterpart) for evaluating the charge current:

$$\begin{aligned}\delta j(\mathbf{R}) = \frac{De}{\pi\nu_0}\mathrm{Im}\int\frac{d\varepsilon}{2\pi}\frac{d\omega}{2\pi}\int d\mathbf{R}'d\mathbf{R}''G^{\mathrm{K}}(\varepsilon\mathbf{R})\mathcal{P}(\omega, \mathbf{R}, \mathbf{R}')\\ \times G^{\mathrm{K}}(\varepsilon - \omega, \mathbf{R}')[U_0(\mathbf{R}' - \mathbf{R}'') - 2\mathcal{F}\bar{U}\delta(\mathbf{R}' - \mathbf{R}'')]\\ \times \nabla_{\mathbf{R}}\mathcal{P}(\omega, \mathbf{R}'', \mathbf{R}).\end{aligned} \tag{23}$$

The two Fock diagrams in Fig. 5 were first formulated and calculated in Ref. [8].

To proceed from Eq. (23) we rewrite G^{K} as $G^{\mathrm{K}}(\varepsilon\mathbf{R}) \approx -2\pi i F(\varepsilon\mathbf{R})\nu_0(\varepsilon)$, where

$$F(\varepsilon, x) = \left(1 - \frac{x}{L}\right)\tanh\frac{\varepsilon - eV/2}{2k_BT} + \frac{x}{L}\tanh\frac{\varepsilon + eV/2}{2k_BT}. \tag{24}$$

In the thermodynamic limit ($V/L \to 0$) and at a finite temperature, one hence reproduces the renowned AA correction

[6] to the linear response conductivity. Nevertheless, at zero temperature and in a finite system, the ε integration in Eq. (23) results in

$$\int F(\varepsilon,x)F(\varepsilon-\omega,x')d\varepsilon = \begin{cases} \frac{2\hbar\omega}{L}(x'-x)+\frac{(eV-\hbar\omega)}{L^2}(2x-L)(2x'-L), & |\hbar\omega|\leqslant eV \\ \mathrm{sgn}(\omega)\frac{2eV}{L}(x'-x)+(eV-\hbar\omega), & |\hbar\omega|>eV \end{cases}. \tag{25}$$

To simplify the remaining spatial integrals, we adopt Eq. (11) again, and the integrals thus reduce to [24]

$$\int_0^L (x-x')\mathcal{P}(\omega,x,x')\frac{\partial}{\partial x}\mathcal{P}(\omega,x',x)dx' = \left[\left(1+\frac{2x^2}{L_\omega^2}-\cosh\frac{2x}{L_\omega}\right)\sinh\frac{2(L-x)}{L_\omega}+x\to(L-x)\right] \times\frac{L_\omega^3}{16D^2\sinh^2(L/L_\omega)} \tag{26}$$

in one dimension. At this point, one notices a drawback of Eq. (23): The value of the thus calculated current explicitly depends on the position x, i.e., a violation of charge conservation. This issue essentially results from the abrupt separation between the long and short range objects in the diagrammatic calculation; in fact, these objects are intertwined. In the numerical formalism below, this issue is resolved by introducing a proper vertex correction to the current operator (see Fig. 8 below). Here, as a partial resolution, one could either take the average value of $j(x)$ or use $j(x=L/2)$ to get an unbiased result. It can be shown that these two approaches will make no qualitative difference in the end. Here we choose the latter approach and thus apply $x=L/2$ to Eq. (26). After rewriting the final ω integral we arrive at

$$\delta I=\frac{(1-2\mathcal{F})eD}{2\pi L^2}\mathrm{Im}\left\{\frac{ieVL^2}{\hbar D}\int_b^\infty\frac{\Upsilon(y)}{y^2}dy-\int_0^b\Upsilon(y)dy\right\}, \tag{27}$$

where $\Upsilon(y)=(1+y^2/2-\cosh y)/\sinh y$ and $b=\sqrt{eVL^2/(i\hbar D)}$. The remaining integrals in Eq. (27) are evaluated numerically, and the $\delta I-V$ curve is plotted in Fig. 6. Evidently, the only relevant energy scale involved in Eq. (27) is the Thouless energy $E_{\mathrm{Th}}=\hbar D/L^2$. Nevertheless, the δI-V curve appears linear over a large range of the ratio eV/E_{Th}, with a slight tendency to bend down at a high eV/E_{Th} ratio. This is in sharp contrast to the situation of $\delta\nu$, whose profile at $eV<E_{\mathrm{Th}}$ is noticeably different than that at $eV>E_{\mathrm{Th}}$. When $eV<E_{\mathrm{Th}}$ the two cusps in $\delta\nu(\varepsilon)$ tend to merge together, since their widths are of the magnitude E_{Th} [see Eq. (18)].

The asymptotic behavior of Eq. (27) is as follows. At high voltages $eV\gg E_{\mathrm{Th}}$, Eq. (27) yields

$$\delta I\approx\frac{(2\mathcal{F}-1)e}{\pi}\sqrt{\frac{DeV}{2\hbar L^2}},\quad eV\gg E_{\mathrm{Th}}, \tag{28}$$

and in the low bias limit, we obtain the correction to linear conductance: $\delta\mathcal{G}=d\delta I/dV\approx 0.4(2\mathcal{F}-1)e^2/h$. If we were to use a bare local potential, i.e., $U_0\approx U\delta(\mathbf{R}_1-\mathbf{R}_2)$, we would instead get

$$\delta\mathcal{G}\approx(0.8e^2/h)U\nu_0. \tag{29}$$

This latter scenario is more relevant to our numerical model to be introduced in Sec. IV A, since the interaction strength will be treated as an input parameter therein. Interestingly, these asymptotic behaviors of δI, derived under the local interaction model, turn out to be very similar (up to a prefactor) to the result of Ref. [8], which was derived with a Debye-screened interaction.

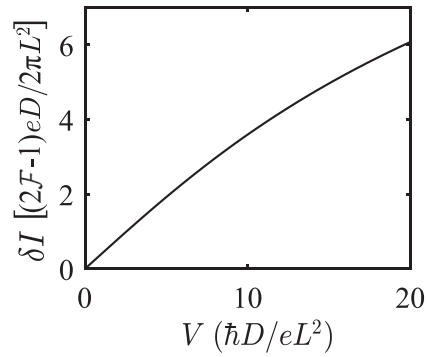

FIG. 6. $\delta I-V$ curve generated from Eq. (27) for a disordered wire at zero temperature. δI is the charge current correction to the first order in e-e interaction.

The result that $\delta\mathcal{G}$ is independent on the system size L signifies a divergence in the linear conductivity $\delta\sigma$ in the $L\to\infty$ limit, since $\delta\sigma=\delta\mathcal{G}\cdot L$ in one dimension. This result is consistent with the original AA theory [6,20], in which the system is assumed to be thermodynamic so that the limit $L\to\infty$ is applied at first, and then the divergence in $\delta\sigma$ is observed as $T\to 0$.

IV. NUMERICAL FORMALISM

In the last section, we analyzed our problem by modeling the system as a continuous disordered medium, where information at the microscopic level only entered through the unperturbed DOS ν_0 and the impurity scattering time τ_0. We also resorted to classical objects such as the diffusion propagator to simplify the diagrammatic calculations. In the following, we shall switch our perspective. We will show how to evaluate the diagrams of Fig. 2 from the numerical point of view where all the given information is atomistic. This development is very important for investigating AA physics in real materials and practical nanostructures. The numerical results to be presented in this section can be understood with the theoretical analyses of the last section.

A. Model

Consider the following general Anderson-Hubbard Hamiltonian:

$$\mathcal{H}=\sum_{i,j}\xi_{ij}c_i^\dagger c_j+\sum_i v_i\hat{n}_i+\frac{1}{2}\sum_{i\neq j}U_{ij}\hat{n}_i\hat{n}_j+\sum_i U_0\hat{n}_{i\uparrow}\hat{n}_{i\downarrow}, \tag{30}$$

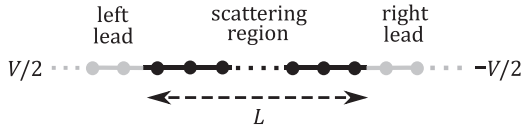

FIG. 7. Schematic diagram of the tight-binding model. Disorder and interaction are confined within the central scattering region. The rest (leads) serves as electronic reservoirs.

where i and j label local atomic orbitals, $c^\dagger$ (c) denotes the fermionic creation (annihilation) operator, ξ_{ij} is a hopping matrix, v_i denotes the on-site potential, and finally, U_{ij} and U_0 denote the intersite and onsite Coulomb interactions, respectively.

For the model system, in the following we consider a tight-binding chain as depicted in Fig. 7. Each atom is assumed to have one single orbital, and electron hopping is restricted between adjacent sites with a uniform hopping amplitude ξ. This leads to a band dispersion $E(k) = -2\xi\cos(ka)$, where a is the lattice constant. Next, disorder is introduced in a sector (marked by black) in the middle of the chain, where the onsite energy of each orbital takes a binary random number (as in binary alloys), i.e., $v_i = \pm v$. A greater v means a higher degree of disorder. The disorder parameter used in our numerical model does not have to follow the weak disorder assumption which we adopted for the analytical derivation. In addition, the e-e interaction is also assumed to be confined within the disordered region, and the rest of the chain (marked by gray) can thus be treated as noninteracting leads whose degrees of freedom can be integrated out using the surface Green's function technique [25]. The voltage bias (V) is applied via shifting the chemical potentials in the respective leads, and the temperature is set at zero in accordance with our theoretical analysis (see Sec. III).

The transformation of the Feynman diagrams (see Fig. 2) into the discrete orbital representation of Eq. (30) is straightforward: One simply replaces the spatial integrals ($\int d\mathbf{r}$) with sums over orbitals ($\sum_i$). Besides, the internal s indices are summed over in a brute force manner, i.e., no simplifications such as Eq. (7) or $\langle G^{\rm R} G^{\rm R}\rangle \approx 0$ are used here. On top of summing over these discrete indices, one also needs to perform a convolution integration over the free energy variable in the diagram. This is done numerically with the trapezoidal method.

The formula for computing the charge current [see Eq. (22)] is discretized as

$$\delta I_i = \frac{2e\xi}{h}\mathrm{Re}\int \delta G^{-+}_{i+1,i}(\varepsilon)\, d\varepsilon. \tag{31}$$

The generalization of Eq. (31) to systems of arbitrary geometries is straightforward [4]. It is important to notice that δG in Eq. (31) actually represents the product $G\Sigma G$, and hence the two Green's functions which eventually meet at the current vertex need to be dressed with a disorder ladder (see Fig. 8). Such vertex correction is essential for ensuring the consistency of the computed current along the model system (i.e., charge conservation). Its effectiveness has been verified in our numerical computations.

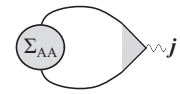

FIG. 8. Diagrammatic representation of the charge current correction [see Eq. (31)] to the first order in interaction. $\Sigma_{\rm AA}$ represents the self-energy diagrams of Fig. 2. Note that the current vertex must be dressed with Fig. 2(c) in order to ensure charge conservation in numerical calculations.

B. Disorder vertices

The Born approximation we used in Sec. III for disorder averaging is not practical for numerical models such as Eq. (30). A more robust algorithm is the CPA, which is henceforth used in our numerical formalism to compute the disorder-averaged NEGFs and the vertex corrections.

The CPA method essentially constructs an effective medium in which the quasiparticle lift time is cut off due to disorder average. The associated medium Green's function and the self-energy (denoted by σ in the following) can be self-consistently solved using the algorithm reviewed in Ref. [26]. Using the self-consistent solution, we introduce the locator object defined as

$$g_i = \left[\sigma_i + G_i^{-1} - v_i\right]^{-1}, \tag{32}$$

where G_i denotes the onsite diagonal of G, and note that g_i is dependent on the disorder configuration through the onsite potential v_i. Now we are in a good position to calculate the high-order kernels which we introduced in Fig. 2. In Ref. [14] we proved that the $K^{(2)}$ kernel should satisfy the local Bethe-Salpeter equation [see Fig. 9(a)], i.e.,

$$K_i^{(2)} = [\langle g_i\rangle * \langle g_i\rangle]^{-1} - [\langle g_i * g_i\rangle]^{-1}, \tag{33}$$

where $*$ denotes an outer product defined as $(f * f)(s_1 s_4, s_2 s_3) = f(s_1 s_3)\cdot f(s_4 s_2)$, and hence $K^{(2)}$ can be viewed as a 4×4 matrix. On the other hand, the $K_i^{(3)}$ kernel is a six-point tensor with 64 elements, and it satisfies the equation diagrammatically shown in Fig. 9(b) [14]. $K_i^{(3)}$ can also be solved by means of linear equations. Note that both $K_i^{(2)}$ and $K_i^{(3)}$, and hence the vertex corrections to the interaction propagator [see Fig. 2(c)], need to be individually calculated at each pair of the energies associated to the vertex. This turns out to be the most time consuming part of our numerical program since the vertex correction is a tensor of

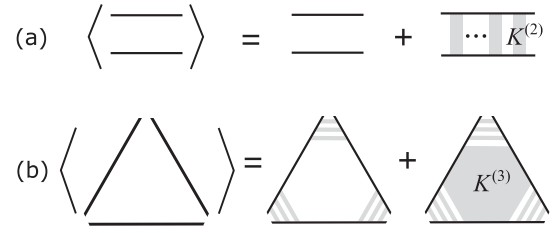

FIG. 9. Diagrammatic representation for the equations used to compute (a) $K_i^{(2)}$ and (b) $K_i^{(3)}$ under CPA. All the objects in the diagrams are local in space. The angle brackets denote disorder average over the random potential v_i. The stripes in (b) denote the ladder series of $K_i^{(2)}$ (see Ref. [14] for more details).

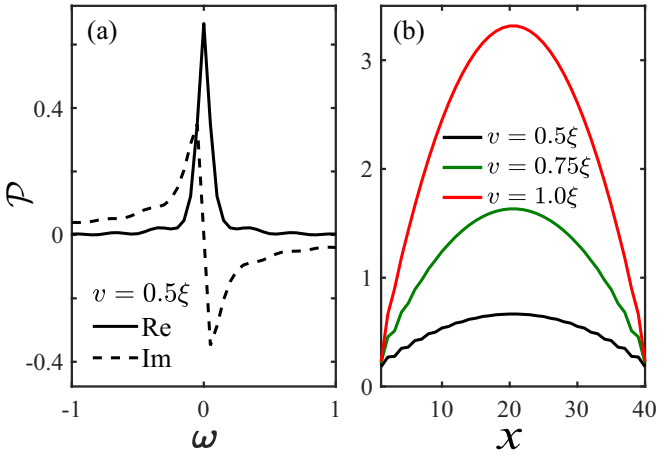

FIG. 10. (a) Numerically simulated frequency dependence of $\mathcal{P}_x(\omega)$, i.e., the diffusive recurrence probability, at the middle of a disordered tight-binding chain ($L = 40a$) sandwiched between ballistic leads. (b) Position dependence of $\mathcal{P}_x(\omega)$ at $\omega = 0$ under a set of differing disorder strengths.

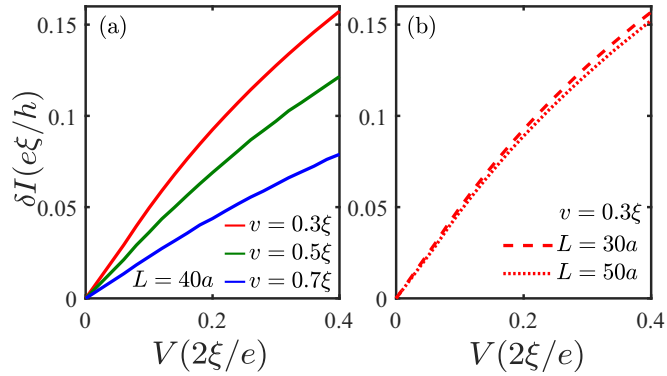

FIG. 11. δI-V relation calculated using the tight-binding chain model [see Eq. (30)] under the setting $U_0 = \xi, U_{ij} = 0$. δI is the current correction to the first order in U_0. (a) The system size is set at $L = 40a$ while the disorder strength is varied by tuning v. (b) Results for another two different system sizes under a given v.

$8N^2$ elements in itself (N being the number of atomic orbitals in the scattering region) and solving for it from the linear matrix equation implied in Fig. 2(c) is $O(N^3)$ complex.

As can be seen from our analysis in Sec. III, the quantity which plays a central role in the AA effects is the diffuson $\mathcal{P}$. It can be verified that our CPA algorithm produces the diffuson correctly. To be concrete, we numerically compute the $\langle G^{\mathrm{R}} G^{\mathrm{A}} \rangle$ correlator using the vertex correction method as demonstrated in Fig. 2(c). The function $\mathcal{P}_x(\omega)$ for a system of 40 sites is plotted in Fig. 10. The frequency dependence of $\mathcal{P}$ at $x = L/2$ is shown in Fig. 10(a), and it clearly displays the causal property one would expect for a typical response function. As discussed in Sec. III A, the peak of $\mathrm{Re}\mathcal{P}_{L/2}$ at $\omega = 0$ is responsible for the DOS anomaly. Figure 10(b) displays the accumulated return probability $\mathrm{Re}\mathcal{P}_x(0)$ along the model chain. Its overall parabolic shape agrees very well with the classical solution [see Eq. (17)]. In addition, the green and black curves in Fig. 10(b) exhibit wiggles in the crossover region between the diffusive wire and the ballistic leads. These wiggles originate from the quantum oscillations in single-particle wave functions subject to impurity scattering. Therefore they are on the scale of Fermi wavelength [27], and the diffuson still remains a smooth function on a length scale greater than the elastic mean free path (l_0). As the disorder strength increases, l_0 approaches the Fermi wavelength or the lattice constant, and thus those wiggles get suppressed [see the red curve in Fig. 10(b)].

C. Numerical results for AA effects

To verify the numerical formalism presented above, we first set the nonlocal interaction $U_{ij} = 0$ in our numerical model [see Eq. (30)], which thus corresponds to the local interaction model as specified in our analytical discussion. Since the local interaction concerns electrons of opposite spins only, the Fock contribution vanishes to the first order in U_0. Thus the parameter setting here corresponds to $\mathcal{F} = 1$ in the analytical formulas.

The typical behavior of the charge current correction for our model system is displayed in Fig. 11. Here the correction δI is computed from Eq. (31) to the first order in U_0. As can be seen, the overall δI-V trend agrees very well with the analytical prediction (see Fig. 6), i.e., it remains almost linear even in the nonlinear transport regime. Its behavior in the linear regime can be explained with Eq. (29), which indicates that the linear conductance is proportional to the unperturbed DOS ν_0. As the disorder strength increases, ν_0 decreases and hence the conductance correction should decrease as well. This relation is well reflected in Fig. 11(a). On the other hand, Fig. 11(b) shows that the conductance correction seems insensitive to the system size. This can be again understood from Eq. (29) since the parameter L is not explicitly involved on the right hand side thereof.

In the following we investigate the AA correction to the DOS profile. As discussed in Sec. III A, the DOS correction is overall dominated by the symmetric part $\delta\nu_1$, which can be well represented by the result at the middle of the chain [see Eqs. (14a) and (18)]. The numerical result from our simulation is displayed in Fig. 12. The solid curves mark the nonequilibrium results obtained under a bias of $V = 0.4\xi/e$. Those obtained under zero bias with otherwise the same system parameters are marked by the dashed curves. Firstly, we notice that the peaks [28] of $\delta\nu$ align very well with the respective Fermi energies of the leads, with the exception of short chains [e.g., the black curve in Fig. 12(b)] whose linear-nonlinear crossover sets in at a much higher bias due to its large Thouless energy. For those curves that clearly display the nonlinear feature, i.e., those with split peaks, their peak values are nearly half of those obtained in equilibrium. This is also consistent with Eq. (14a). Furthermore, the peak values increase with increasing disorder strength [see Fig. 12(a)], and particularly they increase linearly versus the system size L [see Fig. 12(b)]. These observations can be well understood with Eq. (17). To investigate the contribution from the asymmetric part $\delta\nu_2$ [see Eq. (14b)], we plot the full profile of $\delta\nu(\varepsilon, x)$ at a given L and v [see Fig. 13(a)]. In particular we observe that, away from the middle point $x = L/2$, the two peak values of $\delta\nu$ are not equal [see Fig. 13(b)], and that their relative heights [see Fig. 13(c)]

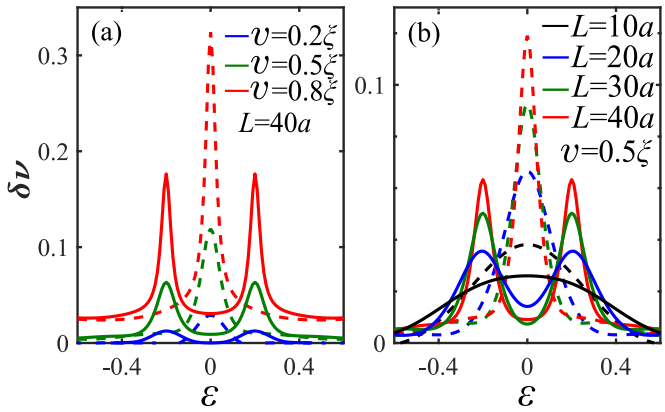

FIG. 12. DOS corrections at the middle of the model chain. The interaction is assumed to be local. The solid lines mark the nonequilibrium results obtained under $V = 0.4\xi/e$. The dashed lines mark the corresponding results obtained in equilibrium (i.e., $V = 0$). (a) The system size L is fixed while the disorder strength v varies. (b) The other way around.

have the x dependence as theoretically predicted in Sec. III A. Besides, we note that the wiggles on the curves of Fig. 13(c) originate from those quantum oscillations in the diffuson [see the black curve in Fig. 10(b)]. Indeed, the atomistic numerical approach allows for capturing details on a microscopic level below the semiclassical scale.

The interesting profile of the DOS correction due to e-e interaction can be experimentally verified by tunnel conductance measurements. To this end, in addition to the two electrical leads, a third probe needs to be added in the scattering region which forms a tunnel junction with the device. Such an experimental setup was demonstrated in Ref. [29] for instance. For a nanostructure, one can use a scanning tunneling microscope as the DOS probe [30,31].

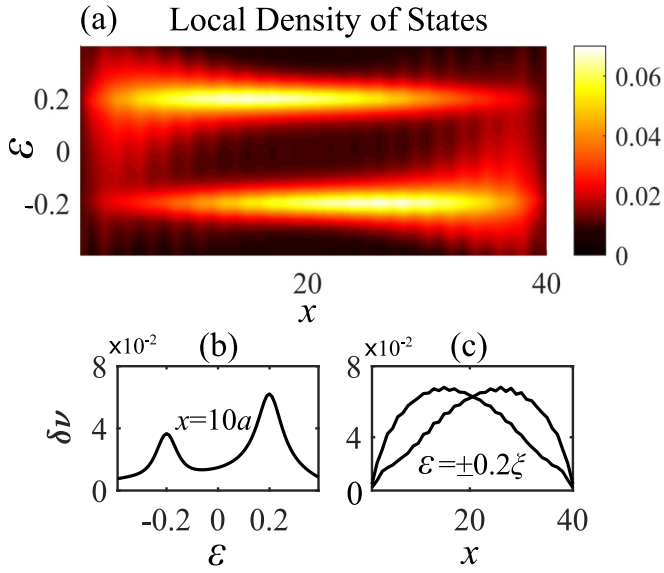

FIG. 13. (a) Complete profile of the local DOS correction as a function of position and energy in a system of $L = 40a$, $U_{ij} = 0$, and $v = 0.5\xi$. (b) Cut at $x = 10a$. (c) Cut at $\varepsilon = \pm eV/2$.

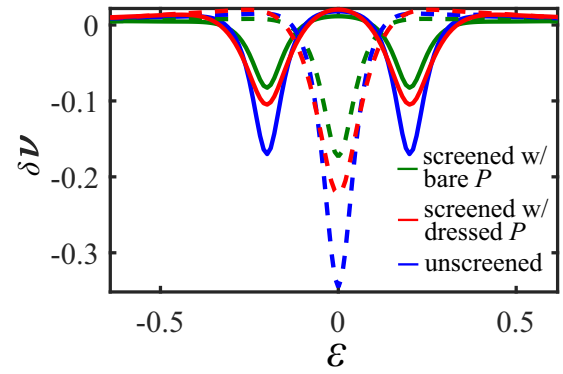

FIG. 14. DOS correction from the Fock contribution (see Fig. 2) at the middle of the model chain ($L = 40a$, $v = 0.5\xi$). The interaction takes the form $U_{ij} = ua/|x_i - x_j|$. Blue curve: The bare interaction U_{ij} is used in the diagram. Red curve: Screening is taken into account via Eq. (5) where the polarization P is dressed with vertex correction [see Eq. (6) and Fig. 2(c)]. Green curve: The screened interaction is calculated with the bare polarization, i.e., without vertex correction. Dashed curves: corresponding equilibrium results.

Although here the DOS correction is demonstrated using a chain model, its generic behavior (as analyzed in Sec. III A) should apply as well to other quasi-one-dimensional wires with a nonzero cross section. However, as the width (W) increases one would expect a decrease in the magnitude of the local DOS correction since the diffusive return probability to a single point decreases. In the limit $W \gg L$ the device becomes virtually a two-dimensional film contact (the contact being one dimensional). As all the diffusion modes with arbitrarily long wavelengths along W are integrated over, the DOS anomaly tends to saturate. These predictions are obtained on a qualitative ground using the relation between the DOS anomaly and the diffuson [see Eq. (14)].

So far we have seen that the numerical results for the local interaction model agree very well with our theoretical prediction. In what follows, we switch to a long-range interaction modeled by $U_0 = 0, U_{ij} = ua/|x_i - x_j|$, which was not accounted for by the theoretical analysis in Sec. III. In particular we shall investigate the effect of many-body screening and the associated energy relaxation effect on the DOS correction in our model system. To this end, we replace the static potential with that calculated from Eq. (5). $U^{\mathrm{R/A/K}}$ is converted to the form $U^{ss'}$, which is then plugged into the diagrams. Figure 14 displays the result calculated for the Fock contribution to the DOS correction [32]. Since the Fock contribution corresponds to $\mathcal{F} = 0$ in Eq. (13), it gives rise to cusps (negative corrections) instead of peaks in the DOS profile. Both the red and the green curves in Fig. 14 are obtained with the screening effect being taken into account. The difference is that for the red curves a dressed polarization [see Eq. (6) and Fig. 2(c)] is used where the disorder vertex correction is included, whereas the bare polarization is used for the green curves. Both results show a screening induced suppression of the DOS correction in comparison to that calculated with the bare interaction (blue curves). We also observe that the screening with dressed polarization (red curves) appears less effective. This reflects

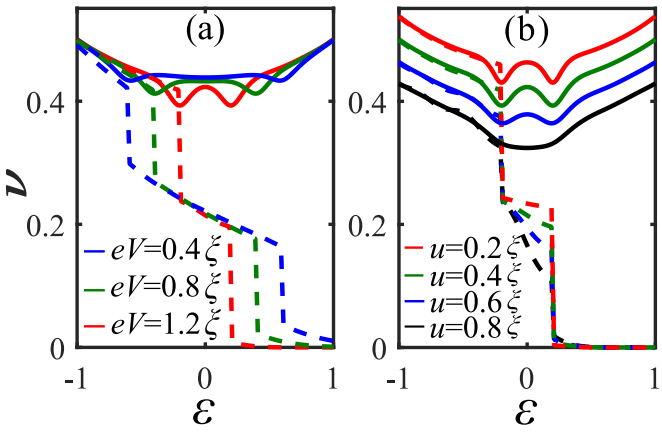

FIG. 15. Energy relaxation effects on the DOS correction under differing bias voltages (a) and interaction strengths (b). The dashed curves represent the energy distribution function extracted from the onsite diagonal of iG^{-+}, which is computed with the self-consistent GW-CPA scheme developed in Ref. [33]. The solid curves are obtained by computing the diagrams of Fig. 2 using the self-consistent Green's functions. The result is presented for a model chain ($L = 40a$) at its middle point. The bare interaction is modeled as $U_{ij} = ua/|x_i - x_j|$.

the fact that diffusion in general tends to hinder the screening process.

To further take into account the energy relaxation effect, one needs to generate a Green's function that reflects the consequence of inelastic scattering. Thus the one-shot algorithm that has been used so far would no more suffice: The self-energy has to be inserted back into the Dyson equation for NEGF [33], and the whole procedure needs to be iterated. To this end, we employ the self-consistent GW-CPA scheme of Ref. [33] and use the thus generated Green's function to compute the DOS correction due to the AA mechanism. The energy relaxation is mainly manifested in the energy distribution function at nonequilibrium [22]. The dashed curves in Fig. 15(a) present energy distributions which we extract from iG^{-+} calculated under a set of different bias voltages. Unlike the step-shaped distribution function in the non-self-consistent case, here we observe a slope within the transport energy window, i.e. $\varepsilon \in (-eV/2, eV/2)$, and a tail at $\varepsilon > eV/2$. The slope which arises from the equilibration process, and the tail which signifies electrons being excited over the Fermi energy, are both signatures of energy relaxation in nonequilibrium transport [22,33]. As the bias increases, the equilibration gets enhanced and the sharp drops in the distribution function are shortened. As a result, the DOS correction is suppressed [see the blue curve in Fig. 15(a)], akin to the situation where the temperature is increased instead of the bias [34]. The effect of increasing interaction strength is twofold. First, it enhances the equilibration process just like the effect of bias increase. This is verified by the dashed curves in Fig. 15(b). Second, the enhanced energy relaxation tends to smear the zero-frequency peak of diffuson, since the diffusive motion of single particles no longer conserves energy in the presence of inelastic e-e scattering. Consequently, as the interaction increases, the two-cusp structure in the DOS profile tends to be smeared [see the black curve in Fig. 15(b)].

V. SUMMARY

We have presented a diagrammatic formalism in the nonequilibrium Green's function framework devised for computing the Altshuler-Aronov (AA) corrections to the electronic structure and transport properties of nanostructures. Importantly, our theory strictly respects the law of charge conservation, thereby featuring the theoretical consistency for transport calculations.

The formalism has been applied to a prototypical Anderson-Hubbard model subject to a nonequilibrium condition. We find that its nonlinear differential conductance decreases slightly as the bias voltage increases and that its overall I-V characteristics appear insensitive to the system size. On the other hand, in the nonlinear regime the interplay between interaction and disorder may induce two peaks or cusps (depending on the interaction model) on the local DOS profile, and their relative heights or depths show an antisymmetric dependence on the position. This finding could be verified by tunnel conductance measurements. We also predict that these anomalous DOS features due to the AA effect tend to be suppressed by inelastic scattering processes. These numerical results are well supported by our theoretical analyses.

This work, together with previous progress [35], allows one to initiate numerical studies of the two most basic quantum corrections: weak localization and AA effects [4], in disordered nanostructures from an atomistic point of view. The remaining tasks include refining the numerical basis set (e.g., linear combinations of atomic orbitals [11] or the muffin-tin scheme [13]) and the computational algorithm, so that real material systems can be efficiently investigated. We hope to be able to report such a work in the future.

ACKNOWLEDGMENTS

We gratefully acknowledge financial support by Natural Sciences and Engineering Research Council of Canada (H.G.). We thank CalcuQuebec and Compute Canada for computational facilities.

[1] D. Belitz and T. R. Kirkpatrick, The Anderson-Mott transition, Rev. Mod. Phys. **66**, 261 (1994).

[2] D. A. Abanin and Z. Papić, Recent progress in many-body localization, Ann. Phys. **529**, 1700169 (2017).

[3] E. Abrahams, P. W. Anderson, D. C. Licciardello, and T. V. Ramakrishnan, Scaling Theory of Localization: Absence of Quantum Diffusion in Two Dimensions, Phys. Rev. Lett. **42**, 673 (1979).

[4] S. Datta, *Electronic Transport in Mesoscopic Systems* (Cambridge University Press, Cambridge, UK, 1997).

[5] G. Zala, B. N. Narozhny, and I. L. Aleiner, Interaction corrections at intermediate temperatures: Longitudinal

conductivity and kinetic equation, Phys. Rev. B **64**, 214204 (2001).

[6] B. L. Altshuler and A. G. Aronov, in *Electron-Electron Interactions in Disordered Systems*, Modern Problems in Condensed Matter Sciences, edited by A. Efros and M. Pollak (Elsevier, New York, 1985), Vol. 10, pp. 1–153.

[7] R. Escudero, J. Lasjaunias, Y. Calvayrac, and M. Boudard, Tunnelling and point contact spectroscopy of the density of states in quasicrystalline alloys, J. Phys.: Condens. Matter **11**, 383 (1999).

[8] K. Nagaev, Nonlinear conductivity of diffusive normal-metal contacts, Phys. Lett. A **189**, 134 (1994).

[9] P. Schwab and R. Raimondi, Quasiclassical theory of charge transport in disordered interacting electron systems, Ann. Phys. **12**, 471 (2003).

[10] D. B. Gutman, Y. Gefen, and A. D. Mirlin, Nonequilibrium Zero-Bias Anomaly in Disordered Metals, Phys. Rev. Lett. **100**, 086801 (2008).

[11] J. Taylor, H. Guo, and J. Wang, *Ab initio* modeling of quantum transport properties of molecular electronic devices, Phys. Rev. B **63**, 245407 (2001).

[12] D. Stradi, U. Martinez, A. Blom, M. Brandbyge, and K. Stokbro, General atomistic approach for modeling metal-semiconductor interfaces using density functional theory and nonequilibrium Green's function, Phys. Rev. B **93**, 155302 (2016).

[13] Y. Ke, K. Xia, and H. Guo, Disorder Scattering in Magnetic Tunnel Junctions: Theory of Nonequilibrium Vertex Correction, Phys. Rev. Lett. **100**, 166805 (2008).

[14] C. Zhou and H. Guo, General theory for calculating disorder-averaged Green's function correlators within the coherent potential approximation, Phys. Rev. B **95**, 035126 (2017).

[15] J. Rammer and H. Smith, Quantum field-theoretical methods in transport theory of metals, Rev. Mod. Phys. **58**, 323 (1986).

[16] D. Vollhardt and P. Wölfle, Diagrammatic, self-consistent treatment of the Anderson localization problem in $d \leqslant 2$ dimensions, Phys. Rev. B **22**, 4666 (1980).

[17] G. Baym and L. P. Kadanoff, Conservation laws and correlation functions, Phys. Rev. **124**, 287 (1961).

[18] F. Vasko and O. Raichev, *Quantum Kinetic Theory and Applications: Electrons, Photons, Phonons* (Springer, New York, 2005).

[19] K. S. Thygesen and A. Rubio, Conserving GW scheme for nonequilibrium quantum transport in molecular contacts, Phys. Rev. B **77**, 115333 (2008).

[20] E. Akkermans and G. Montambaux, *Mesoscopic Physics of Electrons and Photons* (Cambridge University Press, New York, 2007).

[21] J.-J. Lin and J. Bird, Recent experimental studies of electron dephasing in metal and semiconductor mesoscopic structures, J. Phys.: Condens. Matter **14**, R501 (2002).

[22] H. Pothier, S. Guéron, N. O. Birge, D. Esteve, and M. H. Devoret, Energy Distribution Function of Quasiparticles in Mesoscopic Wires, Phys. Rev. Lett. **79**, 3490 (1997).

[23] I. L. Aleiner, B. L. Altshuler, and M. E. Gershenson, Interaction effects and phase relaxation in disordered systems, Waves Random Media **9**, 201 (1999).

[24] Note that the other terms in Eq. (25) that are not linear in $(x - x')$ vanish upon either averaging over x or setting $x = L/2$ by hand, and thus they would not contribute to the final expression of the charge current.

[25] M. L. Sancho, J. L. Sancho, and J. Rubio, Highly convergent schemes for the calculation of bulk and surface Green functions, J. Phys. F: Met. Phys. **15**, 851 (1985).

[26] Y. Zhu, L. Liu, and H. Guo, Quantum transport theory with nonequilibrium coherent potentials, Phys. Rev. B **88**, 205415 (2013).

[27] S. Hershfield, Current conservation and resistance fluctuations in a four probe geometry, Ann. Phys. **196**, 12 (1989).

[28] The peaks observed here correspond to the cusps discussed in Sec. III A. This is due to the $(1 - 2\mathcal{F})$ factor in Eq. (13), which gives a sign flip when $\mathcal{F} = 1$.

[29] A. Anthore, F. Pierre, H. Pothier, and D. Esteve, Magnetic-Field-Dependent Quasiparticle Energy Relaxation in Mesoscopic Wires, Phys. Rev. Lett. **90**, 076806 (2003).

[30] T. Quaglio, F. Dahlem, S. Martin, A. Gerardin, C. Winkelmann, and H. Courtois, A subkelvin scanning probe microscope for the electronic spectroscopy of an individual nano-device, Rev. Sci. Instrum. **83**, 123702 (2012).

[31] S. Bouvron, R. Maurand, A. Graf, P. Erler, L. Gragnaniello, M. Skripnik, D. Wiedmann, C. Engesser, C. Nef, W. Fu *et al.*, Charge transport in a single molecule transistor probed by scanning tunneling microscopy, Nanoscale **10**, 1487 (2018).

[32] The Hartree contribution can be shown to be much smaller than that of Fock when screening is weak [20]. In addition, since the interaction line in the Hartree diagram conserves energy, it concerns static screening only.

[33] C. Zhou and H. Guo, Coulomb drag between quantum wires: A nonequilibrium many-body approach, Phys. Rev. B **99**, 035423 (2019).

[34] F. Pierre, H. Pothier, P. Joyez, N. O. Birge, D. Esteve, and M. H. Devoret, Electrodynamic Dip in the Local Density of States of a Metallic Wire, Phys. Rev. Lett. **86**, 1590 (2001).

[35] C. Zhou and H. Guo, Nonequilibrium dual-fermion approach to electronic transport in disordered nanostructures, Phys. Rev. B **99**, 075414 (2019).